Received: 19 May 2019 | Revised: 6 September 2019 | Accepted: 1 November 2019

DOI: 10.1002/aic.16860

AIChE JOURNAL

TRANSPORT PHENOMENA AND FLUID MECHANICS

Investigating the effect of pressure on a vertical two-phase upward flow with a high viscosity liquid

Mukhtar Abdulkadir[1] | Abolore Abdulahi[2] | Carol N. Eastwick[2] | Barry J. Azzopardi[2] | Ivar E. Smith[3] | Tor E. Unander[3]

[1]Chemical Engineering Department, Federal University of Technology, Minna, Nigeria

[2]Process and Environmental Engineering Division, University of Nottingham, Nottingham, UK

[3]Multiphase Flow Laboratory, SINTEF Petroleum Research, Trondheim, Norway

Correspondence
Abdulkadir Mukhtar, Chemical Engineering Department, Federal University of Technology, Minna, Nigeria
Email: mukhau@futminna.edu.ng

Funding information
Graduate School, University of Nottingham, UK; University of Nottingham; Engineering and Physical Sciences Research Council; Petroleum Technology Development Fund

Abstract

This article presents void fraction and pressure gradient data for sulfur hexafluoride (SF_6) with gas densities of 28 and 45 kg/m^3 and oil (with viscosity 35 times that for water) in a 127 mm diameter pipe. The superficial velocities of gas ranged from 0.1 to 3 m/s and those for liquid from 0.1 to 1 m/s, respectively. Measurements of void fraction data were recorded using a capacitance wire mesh sensor (WMS) system, which permits the 3D visualization of the flow patterns. All the data were obtained with a data acquisition frequency of 1,000 Hz. A differential pressure transducer was used to measure the pressure drops along the length of the pipe. The WMS provide time and cross-sectionally resolved data on void fraction and from an analysis of its output, flow patterns were identified using the characteristic signatures of probability density function (PDF) plot of time series of void fraction. The PDF plots showed the single peak shapes associated with bubbly and churn flows but not the twin-peaked shape usually seen in slug flows. This confirms previous work in larger diameter pipes but with less viscous liquids. For the bubble and churn flows investigated, the pressure gradient was observed to decrease with an increase in gas superficial velocity. Nevertheless, there was an insignificant observed effect of pressure on void fraction below certain transitional flow rates, the effect however became significant beyond these values. In the present work, wisps appear to be smaller, which might be due to the different fluid properties of the working fluids employed. In addition, wisps are easily revealed as long as there is a transition between churn and annular flows regardless of the pressure. Experimental data on void fraction and pressure gradient are compared against existing data. Reasonably good agreements were observed from the results of the comparison.

KEYWORDS
bubbly flow, intermittent flow, pressure gradient, viscous liquid, void fraction, WMS

1 | INTRODUCTION

Effect of pressure has previously been investigated on two-phase gas–liquid flows especially with water that has low viscosity. Most of the work, however, that has been carried out focused mainly on air–water. Hence, most of the available industrial models and correlations have been validated with experimental results from air–water data. In the current study, the effect of pressure on two-phase high viscosity liquid and gas flows had been investigated in a large diameter pipe. Using pressure gradient, rather than void fraction, has been a promising tool for the identification of flow patterns as can be seen in Figure 1. Pressure gradients are easily accessible to measurements

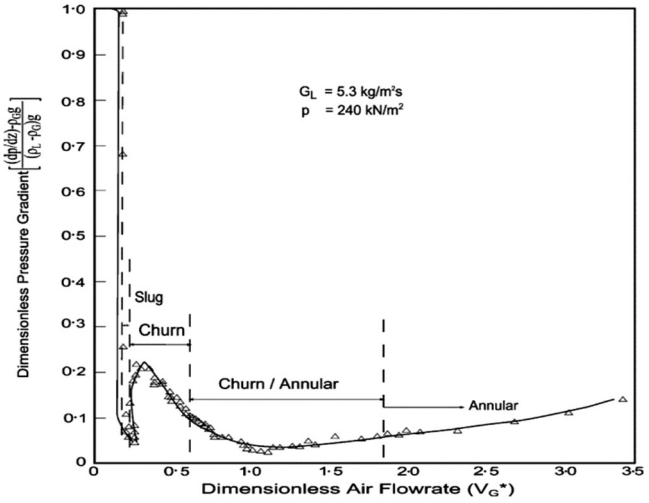

FIGURE 1 Dimensionless pressure gradient as s function of the dimensionless air flow rate in air–water flow in a tube (data obtained by Owen[1] as reported by Hewitt[2])

and may contain sufficient information on the features of flow patterns. The first attempt to relate the fluctuating pressure gradient to flow patterns was that of Nishikawa et al[3] who investigated the statistical properties of static pressures of each flow pattern in upward air–water flow in a 26 mm internal diameter pipe. Frequency distribution and power spectrum density (PSD) function of static pressure signals for different flow patterns were presented. However, the fluctuations of the static pressure signals consist of two parts. One part of the fluctuations is due to the mechanical vibrations of the whole measuring system whilst the other part is due to the flow fluctuation, or void fraction instability, in the measuring section. It is obvious that only the latter fluctuation is related to the flow pattern.

Interestingly, more industries have recently been using large diameter vertical and steeply inclined riser systems to reduce the pressure drop usually experienced with the use of small diameter pipes. As most available data are based on these small diameter pipes, this poses a great challenge for field applications especially in prediction of certain flow characteristics. In effect, evidence shows that flow behavior is greatly influenced by pipe diameters. Hence, in the current study a 127 mm diameter pipe has been employed. In the work by Cheng et al[4] in a 150 mm diameter pipe, no conventional large bubbles that normally occupy the majority of the pipe cross section were observed over the range of flow rates where slug flow would normally appear. Hence, Cheng et al[4] inferred that there is a very gradual transition to a type of churn flow as the gas rate is increased instead of the traditional slug flow in their pipe. In a similar investigation, Ohnuki and Akimoto[5] reported that the churn flow is dominant in large diameter pipes under the same conditions where small diameter pipes have slug flow. They classified the flow patterns observed visually in a transparent pipe as undisturbed bubbly, agitated bubbly, churn bubbly, churn slug, and churn froth. However, this contradicts the previous investigation carried out by other researchers especially with small diameter pipes. For instance,[6-8] suggested that small diameter pipes seem to exhibit bubble, slug, churn, and annular flows for a two-phase gas–liquid flow with increasing void fraction.

2 | EXPERIMENTAL FACILITY

2.1 | Methodology

2.1.1 | Procedure

A schematic diagram of the experimental facility used for the current study is as shown in Figure 2. The experiments were run with sulfur hexafluoride (SF_6) and a mixture of Exxsol D80 and Nexbase 3080. These oil samples were chosen as they are nonflammable, transparent, and nontoxic. Exxsol D80 is a dearomatized aliphatic hydrocarbon oil commonly used in flow loop experiments while Nexbase 3080 is a catalytically hydro-isomerized and dewaxed based oil comprising of hydrogenated, highly iso-paraffinic hydrocarbons. The gas and oil flow rates as well as the oil density were measured by two Coriolis meters. Measurement of the gas density was done through manually weighing a gas sample obtained from the flow loop. A table for the fluid properties is shown in Table 1. The medium flow loop is located at the SINTEF Multiphase Flow Laboratory at Tiller, Trondheim, Norway. Oil in a storage tank was pumped into the test pipe (internal diameter of 127 mm, height of 9 m) using a centrifugal pump while SF_6 was injected with the aid of a compressor into the mixer near the bottom and allowed to flow up through the liquid. The pressure in the test section was initially at 7.5 bar; this was later lowered to 4.5 bar after a series of experiments were carried out at the initial velocity conditions. The velocity of the oil ranged from 0.1 to 1 m/s while that of the gas ranged between 0.1 and 3 m/s. The mixer consisted of an annular section through which the liquid was introduced. This is discussed further in Section 2.1.3. The gas was injected into the mixer through a series of 4 mm holes on the wall of the capped central pipe. The two-phase mixer was mounted at the bottom of the test pipe while the wire mesh sensor (WMS) was located at 6.5 m away from it.

2.1.2 | System test fluid

In this facility, the gas used was SF_6. The gas was initially compressed to a liquefied form at 80 bar in a cylindrical tank. This was sent into the separator (Figure 2) that already contains high viscosity oil mixture (mixture of Nexbase 3080 oil with viscosity of 89 mPa.s and Exxsol D80 oil with viscosity of 1.76 mPa.s). The properties of the fluids are presented in Table 1. The two oil samples were combined to achieve a mixture with a viscosity of 35 mPa.s.

2.1.3 | Gas–liquid mixing section

In the two-phase mixer employed here (Figure 3a) that is similar to those used by several authors,[9-14] the liquid was introduced into a short annulus from the bottom. Gas is then mixed through 4 mm diameter holes at the inner wall of the annulus. The mixture then flows into the main pipe. This design was chosen to: (a) produce

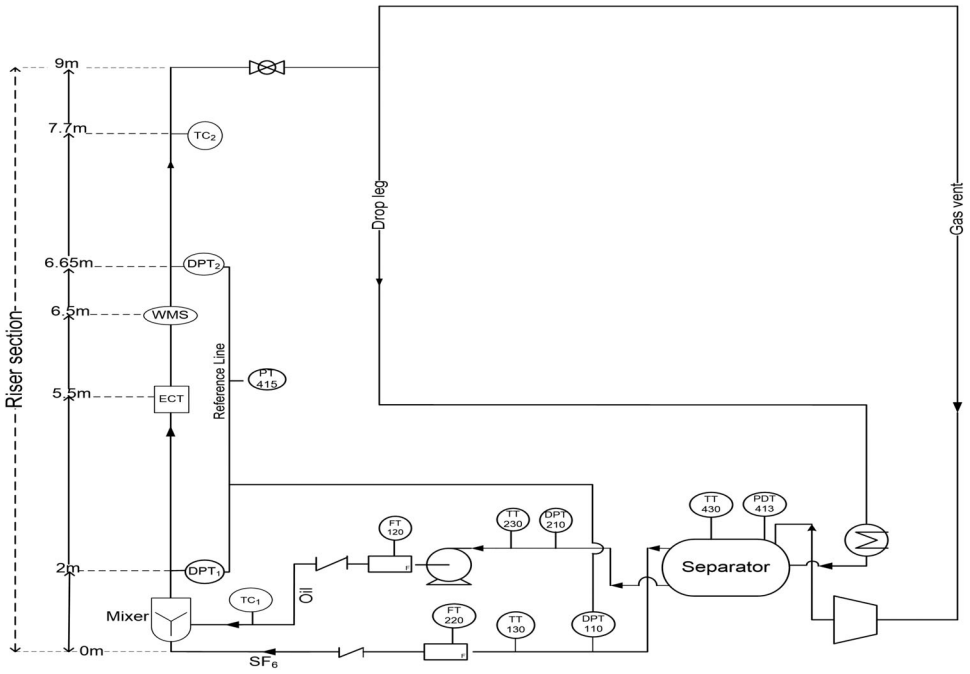

FIGURE 2 Schematic diagram of the experimental flow loop

TABLE 1 Properties of fluid used for experimentation

Type of fluid	Density (kg/m^3)	Viscosity (mPa.s)	Average temperature (°C)
SF_6 gas (at high pressure)	45	0.0151	
SF_6 gas (at low pressure)	28	0.0151	
Liquid mixture (Exxol D80 + Nexbase 3,080)	840	35	22.5

small bubble sizes and (b) to minimize the flow of liquid back into the gas supply line. To avoid liquid from entering the gas injection holes, the shutdown process involves stopping the liquid flow while gas flow is continuously circulated for a few more minutes in order to expel all liquid in the test section. The gas flow is then stopped. The holes were positioned in rings up the pipe with an axial spacing of 20 mm and a circumferential spacing of 16 mm. Alternate holes are staggered to give a triangular array as can be seen in Figure 3b.

2.2 | Instrumentation

2.2.1 | Wire mesh sensor

Many liquid substances like organic liquids and crude oil are nonconducting; this implies that the conductive WMS could not be used in such applications. Thus, a new WMS is required to circumvent such a challenge. It was against this background that a WMS was developed by Da Silva et al.[15] based on the measurement of the electrical permittivity (capacitance), to cover the sensor's capabilities to the detection of nonconducting fluids. It is worthy of mention that a number of papers have been published since 1998 using both options of the WMS. For example, for the conductivity WMS, studies were completed by several authors.[16-23] For the capacitance WMS, Da Silva et al,[15,24-26] Thiele et al,[27] Hernandez-Perez et al,[10] Azzopardi et al,[28] Szalinski et al,[11] Abdulkadir et al[29-31] presented various research studies. WMS have also been deployed for high pressure high temperature, 7 MPa and 290°C, respectively experiments, for example in References 32 and 33.

In this study local time varying void fractions were acquired by using the capacitance WMS transducer developed by Da Silva et al.[15] The 32×32 wire configuration sensor shown in Figure 4 was manufactured by Helmholtz–Zentrum Dresden–Rossendorf (HZDR). It comprises two planes of 32 stainless steel wires of 250 μm diameter, 4 mm wire separation within each plane, and 3 mm axial plane distance. The wires are uniformly distributed over the circular pipe cross-section and in addition the spatial resolution of the images created by the sensor is approximately 4 mm or 820 pixels across the full diameter, which tallies to the wire separation within a single plane. The WMS works at frequencies of 5,000 frames/s that permits small bubbles to be identified. In this work, data were acquired at a frequency of 1,000 frames/s for a 30-s experimental run period. An acrylic frame supports the sensor and permits fixation into the text flow pipe section.

It is worthy of mention that an associated electronic sensor measures the local permittivity in the gaps of all crossing points by successfully applying an excitation voltage (sine wave of 5 MHz) to each one of the sender electrodes at one wire plane while measuring in parallel the current flowing toward receiver electrodes at the other wire plane. The nonactivated transmitter wires are grounded. This step guarantees that the electrical field distribution is concentrated along the activated wire and permits for a sampling of only a well-defined section within the pipe, so that the measured currents are explicitly related to the corresponding crossing point. For the permittivity measurements, a sinusoidal alternating voltage is applied and a demodulation scheme is

subsequently applied. After digitizing, the measured data are sent to a computer where they are processed and displayed. The method is able to generate up to 7,000 images per second. Details of the electronic circuits used may be found in Reference 26.

There are two main intrusive effects of WMS on bubbles in the two-phase flow. The first one is the bubble break-up. The second one is the bubble deceleration. Wangjiraniran et al[34] investigated the change of bubble flow with liquid superficial velocities of 0.1 and 0.2 m/s using a WMS. They found that the bubbles were decelerated by about 40–50% compared to the bubble velocity upstream of the sensor. Later, Fuangworawong et al[35] studied the intrusive effects of a WMS in a counter-current bubble flow, and they observed a similar bubble deceleration. Ito et al[36] sustained the research in this line by deploying a WMS to estimate the bubble velocity of an air–water bubbly flow in a vertical channel with a square cross section. They found that the bubbles were strongly decelerated when they collide with the wire grids in case of low liquid superficial velocities. They concluded that the effect decreases with increasing liquid velocity and finally turns into a slight acceleration that corresponds to the degree of the cross-section obstruction by the wires.

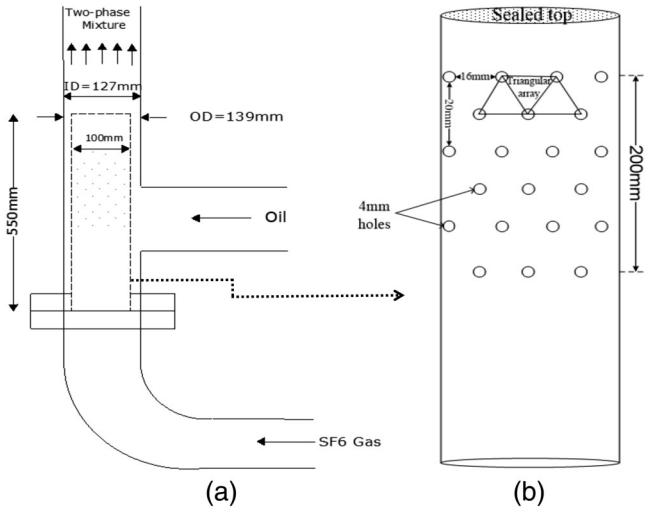

FIGURE 3 Two-phase mixing configuration showing (a) layout of the gas injection unit and (b) two-phase flow mixing point

Ito et al[36] thereafter provided an excellent explanation for the acceleration and deceleration of the bubbles in terms of the Weber number (*We* = inertia forces/surface tension forces). That the inertia of the liquid stabilizes the bubble shape and presses the bubble through the wire grids against the action of superficial forces. At low liquid superficial velocities, the surface tension effects dominate over inertia forces. Accordingly, decelerating forces during the contact of the gas–liquid interface with the solid surface of the electrode wires dominate and the bubble is decelerated.

Based on WMS's strong spatial resolution, it enables data such as bubble size distributions to be extracted. Hence, WMS can provide details of the distribution of bubble sizes present; this can be both overall and time resolved.

2.2.2 | Differential pressure transducers and thermocouples

Figure 2 shows a differential pressure transducer (DPT) with a range of 0–2.5 bar and nominal pressure of 16 bar and an accuracy of ±0.25%, output voltage of 1 to 5 V and a data acquisition frequency of 1,000 Hz that was used to measure the pressure drop in this work. The model number of the DPT is 730-E-2501-1-5-100-J00-1-000 and was made by Impress Sensor and Systems. Both the sensitivity and range were taken into consideration in the selection of the DPT. The DPT was used to measure the time varying two-phase total pressure drop across the test section. In order to achieve this, two pressure tapping were provided, located in the vertical pipe. The particular axial locations of the tappings as depicted in Figure 5 are 2 and 6.65 m from the foot of the test section. Hence, the total pressure drop was measured concurrently with the void fraction.

Before the commencement of making measurements of pressure drop, the DPT had to be calibrated. One of the advantages is having zero span features that make them easy to calibrate. Although the DPT used in the experiment was factory calibrated with a calibration certificate provided to the user, a second calibration was conducted on the transducers to confirm the accuracy of the previous calibration.

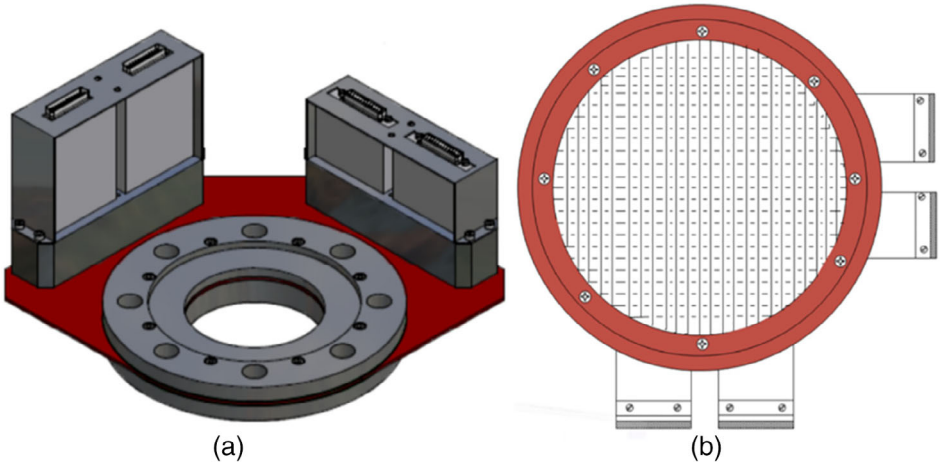

FIGURE 4 (a) Wire mesh sensor (WMS) used during experimentation. (b) 32×32 wire mesh sensor for pipe measurement [Color figure can be viewed at wileyonlinelibrary.com]

The calibration exercise carried out established the link between the output voltage of the DPT and the differential pressure.

The DP transmitters were calibrated against static liquid columns up to 3 mm in length by filling a vertical transparent tube with water at a temperature and density of 20°C and 998 kg/m^3, respectively. The transparent tube used for calibration was made of polycarbonate material. It was scaled from zero using a special scaled tape for that purpose. The high pressure inlet port (DPT_1) of the DPT was connected to the water column, while the lower inlet pressure (DPT_2) was sealed.

It is worthy of mention that for accurate pressure drop measurements, it is essential for the pressure tappings to be purged frequently. Otherwise, pressure fluctuations will introduce a two-phase mixture into the DPT lines triggering incorrectness in the measured pressure drop as a consequence of surface tension effects and indefinite hydrostatic head. It was against this backdrop that a purging system using the venting valves was used to keep an uninterrupted liquid line to the DPT from the pressure tapings. The output voltage from the DPT was recorded using a digital multimeter (MASTECH M-830BZ).

The calibration was started by zeroing the DPT at the lowest level of the water column. The voltage recorded was 1 V at that point. The height of the water was then gradually increased by adding small volume of water in steps to the column from the tap. Thus, the corresponding changes observed of the water level to the output voltage were recorded until it reached the highest level, that is, output voltage of 5 V. The change of the output voltage was then plotted against the water static head to obtain the calibration for each DPT. The calibration curve is shown in Figure 6. Figure 6 shows the plot of the results from calibration that perfectly matches those provided by the manufacturer. The equation in the plot was programmed into LabVIEW to generate instantaneous pressure gradient.

Two T-type thermocouples, TCl and TC2, were inserted into both the liquid inlet and the two-phase flow outlet of the pipe, respectively, as shown in Figure 2 to ensure that temperature data are logged in order to monitor and control the temperature. As changes to temperature can affect density, viscosity, surface tension, and other physical properties of the fluid. It therefore became imperative for the thermocouples to be calibrated to ensure accurate determination of temperature.

The calibration of these thermocouples was done using ice, hot and boiling water. A thermometer was inserted into each system (ice cubes, hot and boiling water) to measure the temperature. This temperature measurement with the aid of a mercury thermometer which has an accuracy of ±1°C was simultaneously taken alongside the voltage readings using a digital multimeter. Figure 7 shows the plot of the temperature versus voltage with a line of best fit. The equations of these lines (calibration equations) were programmed into LabVIEW to obtain the temperatures of the two-phase flow at the liquid inlet at the bottom end as well as at the two-phase flow outlet of the pipe.

3 | RESULTS AND DISCUSSION

The flow rates at which measurements were made correspond to gas superficial velocities in the range 0.1–3 m/s and liquid superficial velocities of 0.2 to 1.0 m/s. Figure 8 shows the experimental operating points of the present study described in a flow pattern map (Figure 8) generated using the FLOPATN computer code developed by Pereyra and Torres.[37] From an analysis of the observations it is concluded that the Pereyra and Torres[37] model predicts bubble and churn flows accurately. For each run, data was taken at a rate of 1,000 cross-sections per second for 30 s. Measurements were taken

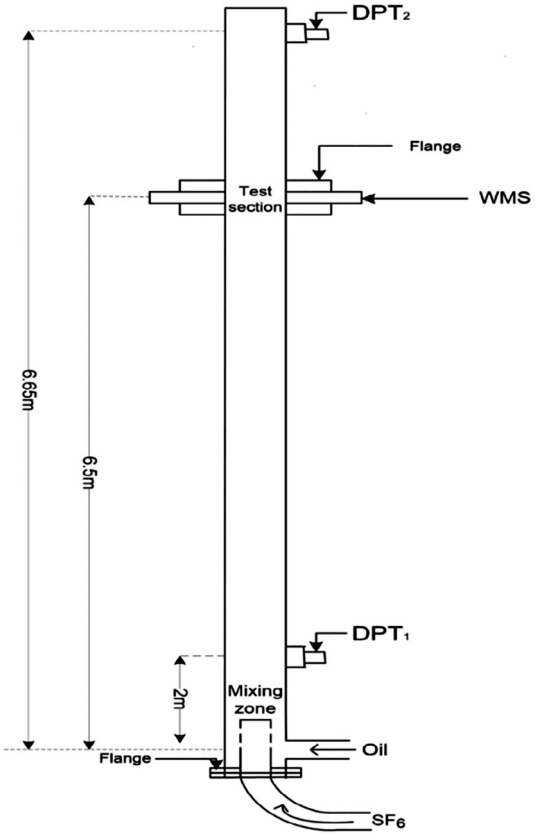

FIGURE 5 Positions of the measuring instruments along the pipe

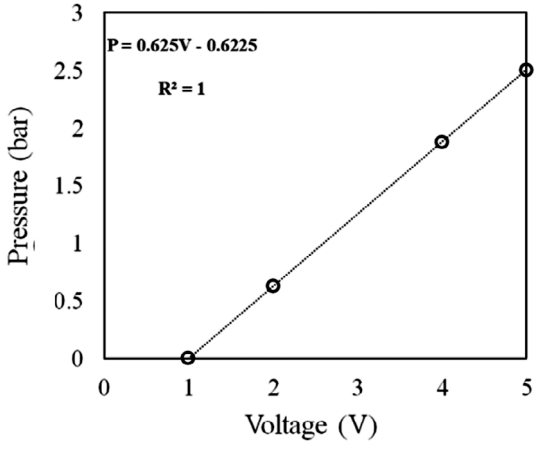

FIGURE 6 Calibration of the differential pressure transducers

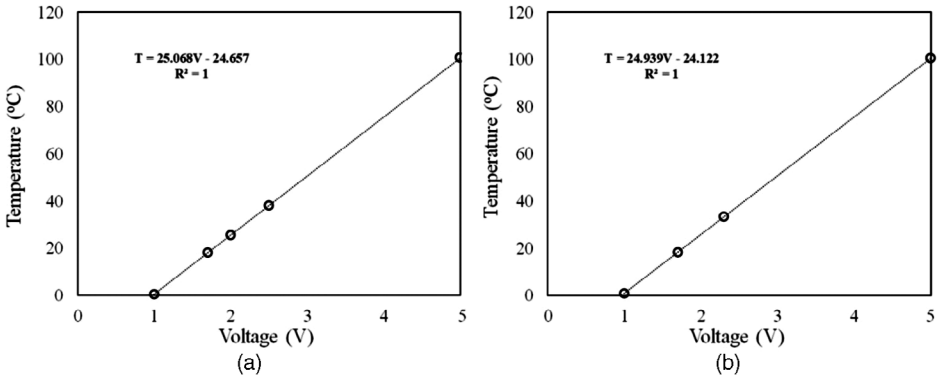

FIGURE 7 Calibration plots for the thermocouples (a) at the liquid inlet at the bottom end of the pipe (TC1). (b) At the two-phase flow outlet of the pipe (TC2)

with the pipe full of oil and full of gas before and after each batch of tests to obtain and check the calibration.

3.1 | Power spectral density (PSD) and dominant frequency

Gregory and Scott[38] developed a correlation for predicting slug frequency based on the data by Hubbard.[39] Owing to the fact that higher viscosity liquid has been used for the current study that shifts the transition between flow regimes, a different approach has been used to obtain the dominant frequency in order to account for changes in viscosity. To determine this dominant frequency of periodic structures, the methodology of PSD as defined by Bendat and Piersol[40] was applied. Hubbard and Dukler[41] used PSD of pressure fluctuation to identify flows such as separated, dispersed, and intermittent flows for horizontal pipes. PSD according to Abdulkadir et al[13] is a measure of how the power in a signal varies over a range of frequency and thus, it defines how the power (or variance) of a void fraction time series is distributed with frequency. Mathematically, it is defined as shown in Equation (1) as the Fourier Transform of the autocorrelation sequence of the time series. The method presents the PSD functions in terms of direct Fourier Transformations of the original data. The auto covariance function of a signal *x(t)* is given by:

$$R_{xx}(k\Delta\tau) = \frac{1}{T-\tau}\int_0^{T-\tau} [x(t)-\bar{x}].[x(t+k\Delta\tau)-\bar{x}]dt; \tau < T \quad (1)$$

where T is the sampling period, $k\Delta\tau$is the time delay, $\tau$is the interrogating time delay and

$$\bar{x} = \frac{1}{T}\int_0^T x(t)dt \quad (2)$$

PSD is then obtained from:

$$P_{xx}(f) = \Delta\tau\left(\frac{1}{2}R_{xx}(0) + \sum_{k=1}^{\tau/\Delta\tau-1} R_{xx}(k\Delta\tau)W(k\Delta\tau)Cos(2\pi fk\Delta\tau)\right) \quad (3)$$

where $w(k\Delta\tau)$is a windowing function. Windowing function according toHernandez–Perez et al[10] helps to suppress the spectrum leakage that frequently comes out as the sidelobes at high frequency end of the spectrum. By using a suitable windowing function, the frequency contributing to the system becomes obvious. In the analysis carried out here to determine the dominant frequency, a basic cosine windowing function as depicted in Equation 4 was used,

$$w(k\Delta\tau) = \cos\left(\frac{\pi k\Delta\tau}{2\tau}\right) \quad (4)$$

With the aid of the PSD analysis, it is possible to distinguish between periodic and chaotic responses. It is known that for a chaotic motion, the power spectrum is a continuous process. As the intermittent region of a two-phase flow is regarded as a chaotic region, PSD analysis is a useful tool in identifying flow regimes. In effect, its characteristic features at different pressure levels can be identified when compared. Hence, the transition from smooth to chaotic flows can be identified through the PSD signatures as shown in Figures 9a–d. At low gas superficial velocities, the harmonic signal response was more chaotic than at higher gas superficial velocities. This is probably due to the response to changes from bubbly to intermittent flows.

In general, the dominant frequency can be observed in Figure 10a to increase with an increase in liquid superficial velocity. However, the trends for the variation of dominant frequency with pressure are quite irregular in particular at low gas superficial velocities. These can be attributed to changes in flow pattern. Similar observation has been reported by Szalinski et al[11] and Abdulkadir et al.[13]

A good way to describe the dominant frequency of periodic structures is in terms of Strouhal number (fD_t/u). The plot of gas-based Strouhal number against Lockhart-Martinelli parameter as depicted in Figure 10b show that both present data and most of the other data lie on a parallel line. This is expected as Gokcal et al[42] reported that there was a distinct extra effect of viscosity in their data that was for horizontal pipes.

By plotting gas-based Strouhal number against the product of the dimensionless inverse viscosity number and velocity ratio as proposed by Gokcal et al[42] to account for viscosity effect (see Figure 10c), the data in the present study were compared with data of Szalinski et al.[11] The data show very good agreement.

3.2 | Flow structures

The flow structures, as revealed by the WMS are illustrated in Figure 11a,b at high and low pressures, respectively. The information

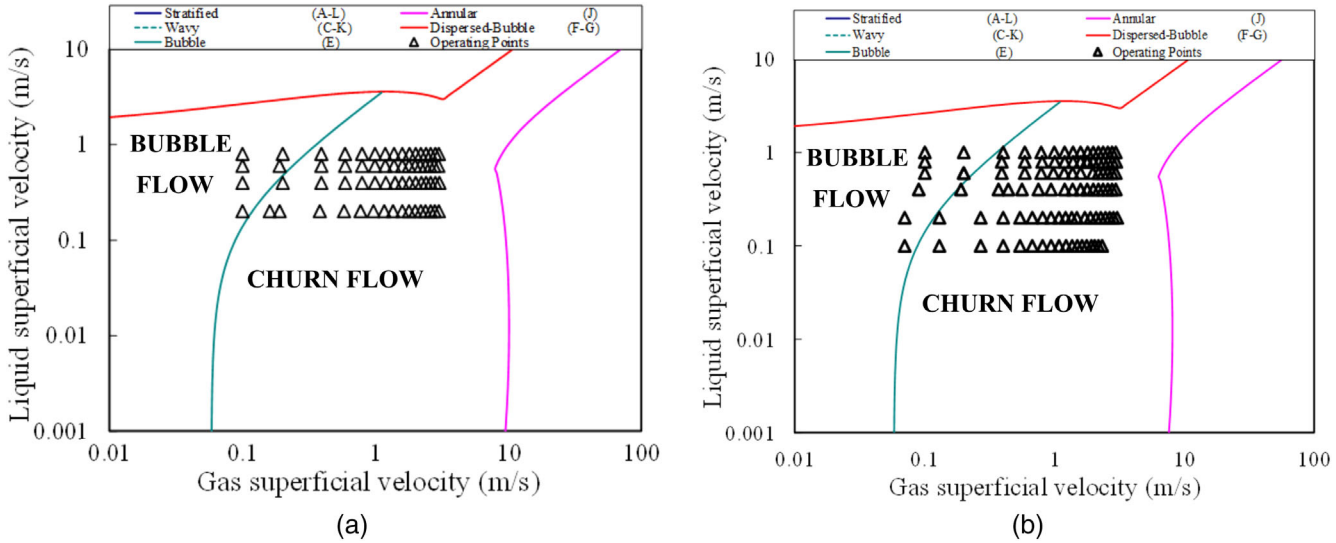

FIGURE 8 Flow pattern map under current experimental conditions predicted by Pereyra and Torres[37] [Color figure can be viewed at wileyonlinelibrary.com]

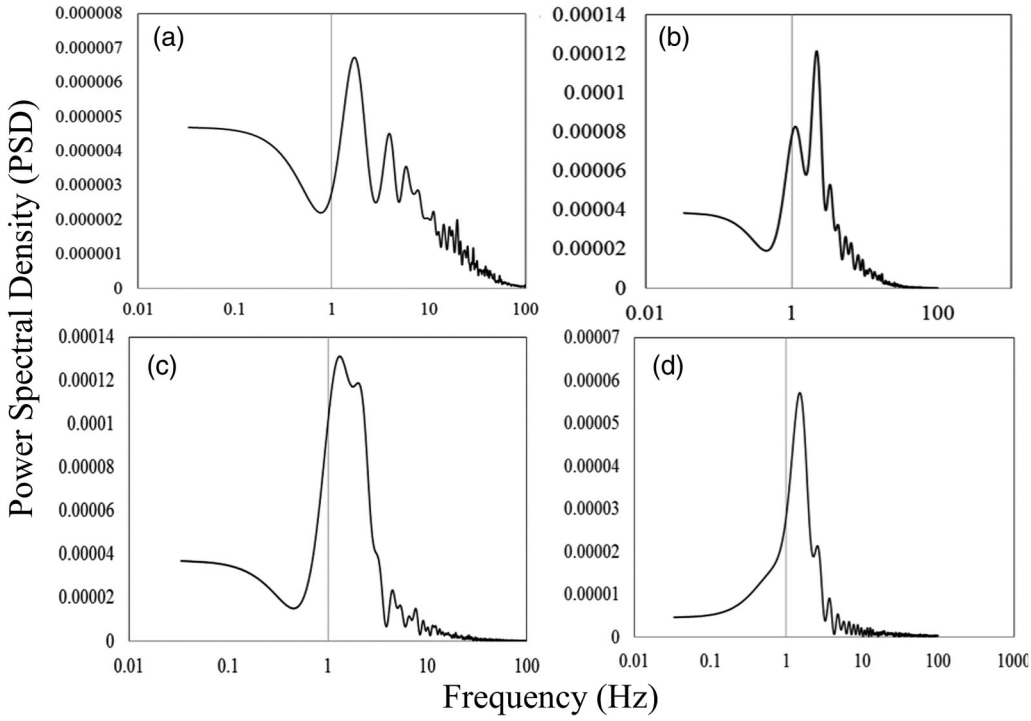

FIGURE 9 PSD and dominant frequency plots at liquid superficial velocity of 0.4 m/s and gas superficial velocities (m/s): (a) 0.1, (b) 0.6, (c) 1.0, (d) 2.0

is held in the form of pixels of 4 × 4 mm. These are colored according to the amount of liquid or gas within the area. In these, the reddish-brown represents 100% gas while blue is 100% liquid. Light blue, orange, and yellow represent intermediate phases. It can be observed that at low-gas superficial velocities, there are no significant changes in bubble distribution.

It can be observed from Figure 12 that at liquid and gas superficial velocities of 0.2 and 1.0 m/s, respectively, a number of drops that appear in yellow/light green color (low region) but do not occupy the whole of the individual pixel can be seen. Also seen on the plot are high regions occupied by gas that appear in red color. They may be regarded as parts of churn flow (huge waves). The low and high regions can be associated directly with the more easily recognizable features in the time series and PDF of void fraction shown in Figure 12a,b. On the matter of time series of void fraction (Figure 12a), periodic fluctuations in void fraction though not regular between 0.7 and 0.4 can be observed on the time trace. The PDF of void fraction, Figure 12b, shows a single peak at a void fraction

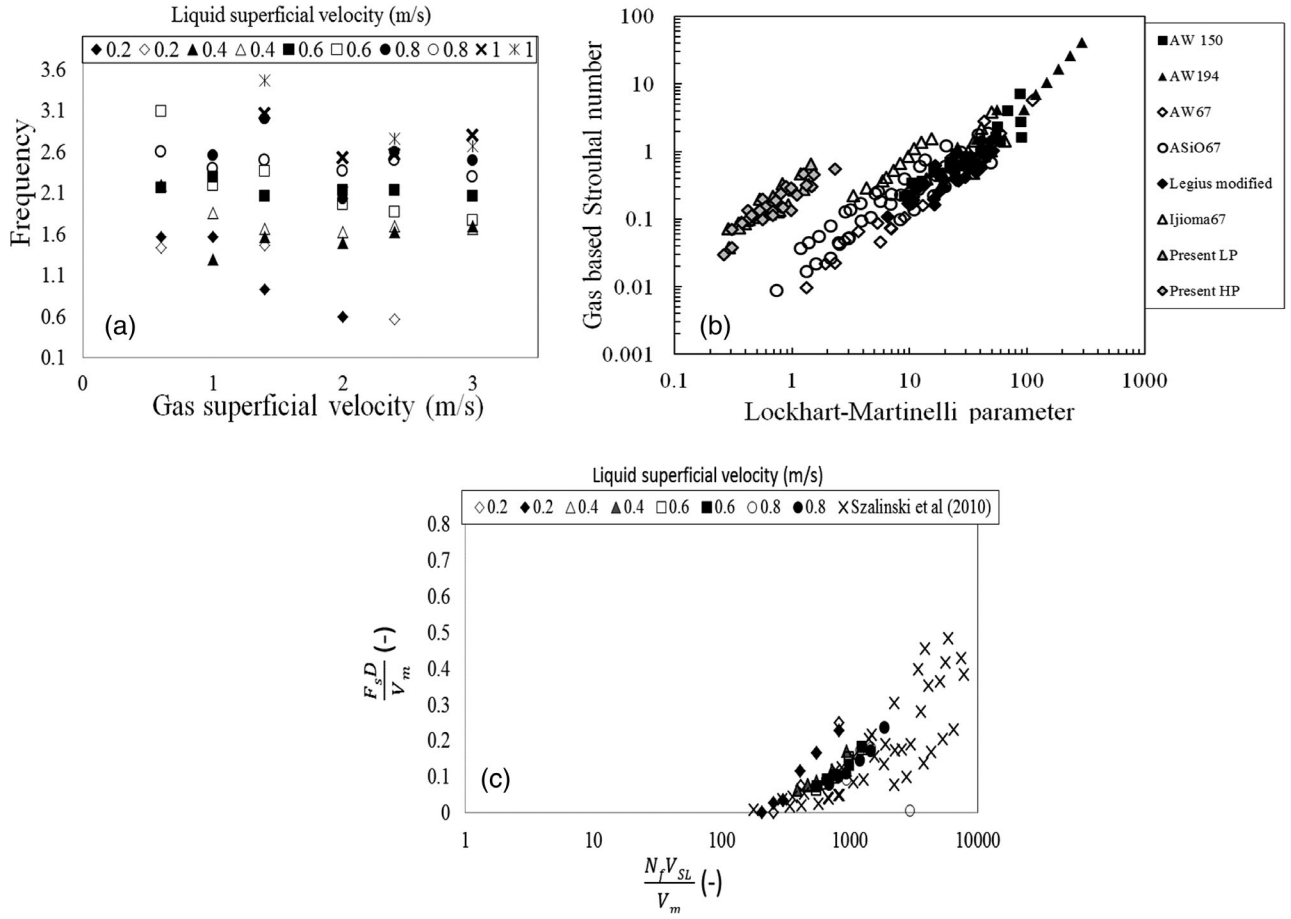

FIGURE 10 (a) Dominant frequency of periodic structures as derived from power spectral density (PSD) analysis: closed symbols and x = high pressure, open symbols and x = low pressure. (b) Gas-based Strouhal number versus Lockhart-Martinelli parameter. (c) Gas-based Strouhal number versus inverse viscosity number and velocity ratio

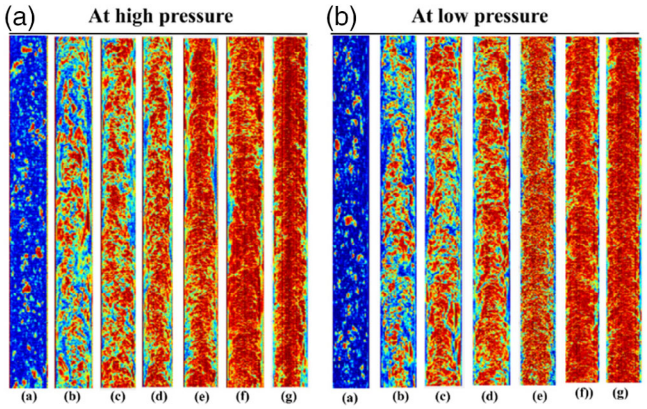

FIGURE 11 Visual side view of wire mesh sensor (WMS) at A-High pressure: liquid superficial velocity = 0.4 m/s; gas superficial velocity = (a) 0.1, (b) 0.6, (c) 1.0 (d) 1.4, (e) 2.0 (f) 2.4, (g) 3.0 m/s and at B-Low pressure: liquid superficial velocity = 0.4 m/s; gas superficial velocity = (a) 0.1, (b) 0.6, (c) 1.0 (d) 1.4, (e) 2.0 (f) 2.4, (g) 3.0 m/s [Color figure can be viewed at wileyonlinelibrary.com]

of 0.6, but with a base spanning from 0.7 to 0.4. This characteristic signature according to Costigan and Whalley[8] is churn flow. In addition, the PDF of void fraction shows that we have large wisps of liquid and the product of incomplete atomization. Wisps are continuous ligaments of liquid flowing in the center of the pipe. A similar observation is also seen in Figure 13 at same liquid superficial velocity of 0.2 m/s but at a higher gas superficial velocity of 1.4 m/s.

This is not to dispute the existence of wisps at low pressures but to inform the readers about how wisps are easily revealed as long as there is a transition between churn and annular flows regardless of the pressure. Interestingly, wisps were observed by Hernandez–Perez et al[10] and Sharaf et al[43] at the same liquid superficial velocities. However, in the present work, the wisps appear to be smaller, which might be due to the different properties of the working fluids employed. It was against this background that a comparison between the wisps frequencies obtained from present work against those obtained by Hernandez–Perez et al[10] and Sharaf et al[43] are presented and discussed in Section 3.3.

3.3 | Further analysis of wisps

As wisps were observed in the current work as earlier reported in Section 3.2, it therefore became necessary to plot the frequencies of these wisps and compare against published data. This plot is shown in Figure 14.

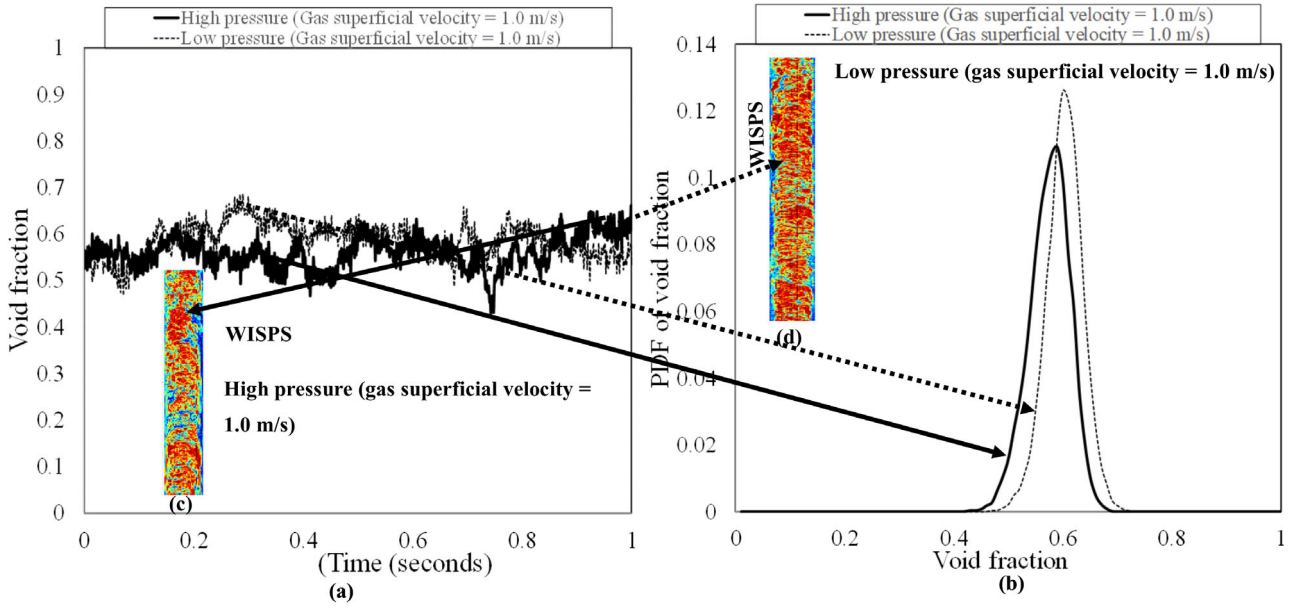

FIGURE 12 (a) Time series of void fraction at high and low pressures of 7.5 and 4.5 bars, respectively. (b) PDF of void fraction at high and low pressures of 7.5 and 4.5 bars, respectively, (c) visualization of wire mesh sensor (WMS) data at high pressure of 7.5 bar, and (d) visualization of wire mesh sensor (WMS) data at low pressure of 4.5 bar. Liquid and gas superficial velocities of 0.2 and 1.0 m/s, respectively. Blue region represents liquid/oil while the red region represents gas, SF_6 [Color figure can be viewed at wileyonlinelibrary.com]

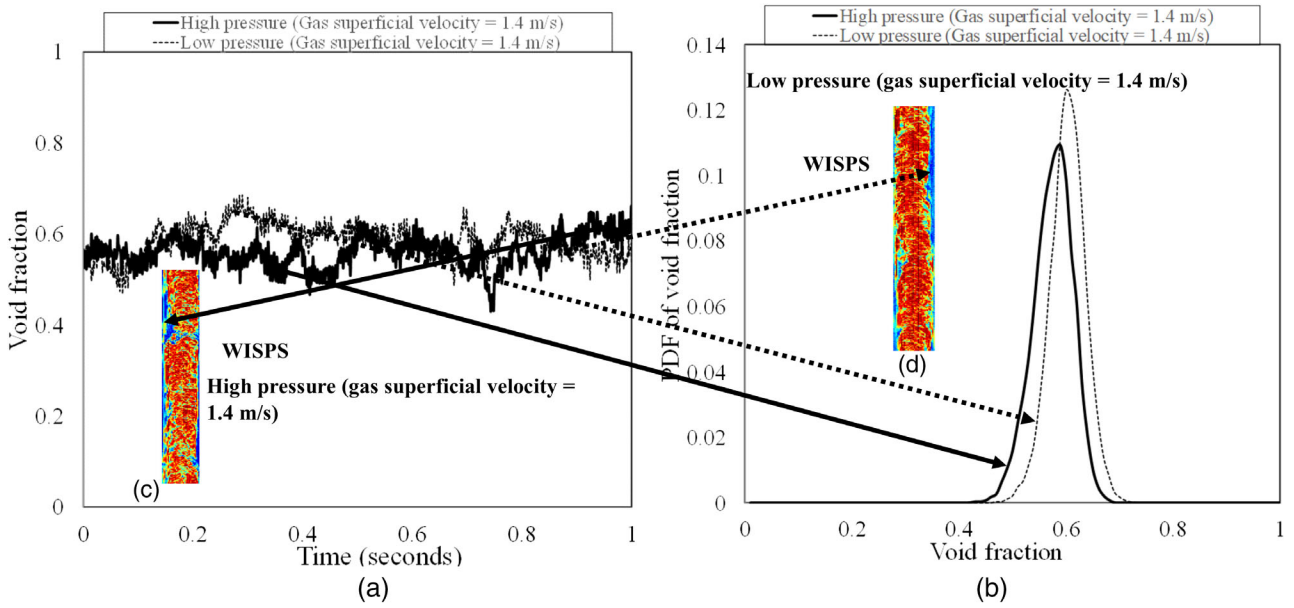

FIGURE 13 (a) Time series of void fraction at high and low pressures of 7.5 and 4.5 bars, respectively, (b) PDF of void fraction at high and low pressures of 7.5 and 4.5 bars, respectively, (c) visualization of wire mesh sensor (WMS) data at high pressure of 7.5 bar, and (d) visualization of wire mesh sensor (WMS) data at low pressure of 4.5 bar. Liquid and gas superficial velocities of 0.2 and 1.4 m/s, respectively. Blue region represents liquid/oil while the red region represents gas, SF_6 [Color figure can be viewed at wileyonlinelibrary.com]

The wisp frequency was obtained by counting the wisps observed in the side view images reconstructed from the WMS. This is to avoid confusion with the dominant frequency obtained while using the method of PSD, due to other flow structures that are present, particularly huge waves.

It can be observed from Figure 14 that the wisps frequency increases with an increase in gas superficial velocity. This is in good agreement with those observed by Sharaf et al[43] but vary from those observed by Hernandez–Perez et al.[10]

As the viscosities of the fluids for all cases compared in Figure 14 vary, it is more logical to make comparison based on these viscosity changes. Figure 15 expresses wisps frequencies in terms of dimensionless numbers with consideration given to viscosity changes. In general,

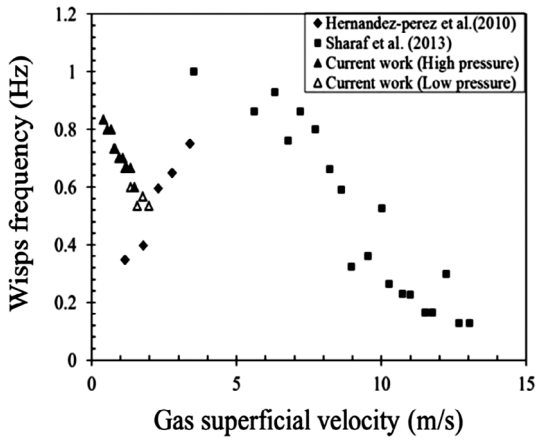

FIGURE 14 A plot of wisps frequency from present study against data from Sharaf and van der Meulen[43] and Hernandez–Perez et al[10] at various gas superficial velocities

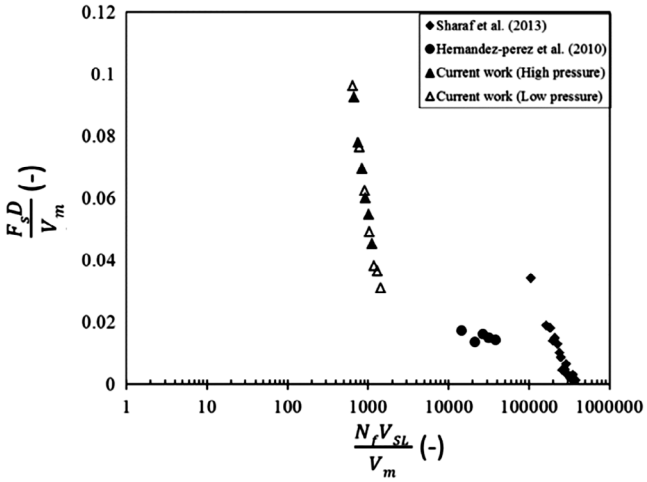

FIGURE 15 Dimensionless numbers plotted and compared with data from Sharaf and van der Meulen[43] and Hernandez–Perez et al[10]

the observed trends as shown in Figure 15 are seen to show the same tendency especially against the work of Gokcal et al.[42] This is not surprising as Sharaf et al[43] and present work used same 127 mm diameter pipe.

When the differences in gas superficial velocities are analyzed in terms of Weber number, the resulting plots show a good agreement with the work by Sharaf et al[43] as can be seen in Figure 16. It is observed from Figure 16 that the value of the ratio of wisps frequency (f_w) and the dominant frequency (f) against Weber number is high at low Weber number for the work of Sharaf et al[43] compared to the present study. This may be attributed to the viscous effect of the liquid on the bubble coalescence process.

3.4 | Bubble size distribution

The bubble size distribution has been obtained from further analysis of the 3D void fraction data. It is performed using an extended decremental recursive fill algorithm developed by Prasser and Beyer.[44] The bubbles were identified by extracting the contribution of each statistical bubble diameter bin to the overall void fraction.

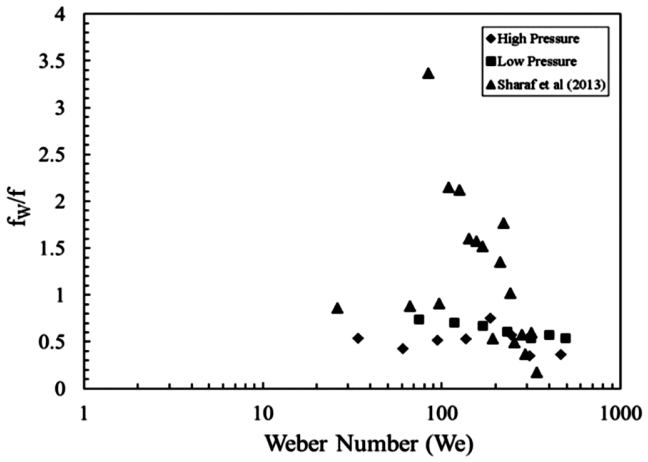

FIGURE 16 Ratio of wisps frequency to dominant frequency against Weber number for both low and high pressure compared with data from Sharaf and van der Meulen[43]

The bubble size distribution is given as:

$$h(D_b) = \frac{d\varepsilon}{dD_{bubble}} \tag{5}$$

Using the bubble volume, the corresponding equivalent bubble diameter D_{bubble} is calculated as

$$D_{bubble} = \sqrt[3]{\frac{6}{\pi} V_{bubble}} \tag{6}$$

Details on the methodology for extracting bubbles size information from WMS data can be found in Prasser et al.[16] Bubble size distributions for selected gas superficial velocities and at liquid superficial velocities of 0.2, 0.4, 0.6, 0.8, and 1.0 m/s are shown in Figure 17. They are constructed by summing the contribution of the bubbles of a given range of diameters to the integral volumetric gas fraction. The partial gas fractions $\frac{d\varepsilon}{dD_{bubble}}$ are plotted against the equivalent bubble diameter D_{Bubble}. It can be observed in Figure 17 that at the lowest liquid superficial velocity 0.2 m/s, the effect of pressure can be seen based on the appearance of smaller bubbles at a higher pressure of 7.5 bar. However, as the liquid superficial velocity is increased, the size of the bubble distribution become bigger at a low pressure of 4.5 bar.

3.5 | Pressure effect on mean void fraction

It can be observed from Figure 18a,b that at low liquid superficial velocities, the effect of pressure on mean void fraction is insignificant. This effect however begins to manifest with an increase in liquid superficial velocity as depicted in Figure 18c, d. This is in particular occurs at critical gas and liquid superficial velocities of 1 m/s and 0.6 m/s, respectively. Beyond this liquid superficial velocity, the effect of pressure on mean void fraction at high pressure is bigger than at low pressure.

It is worthy of mention that as pressure is directly proportional to density, it follows that an effect of pressure will trigger a correct effect of density.

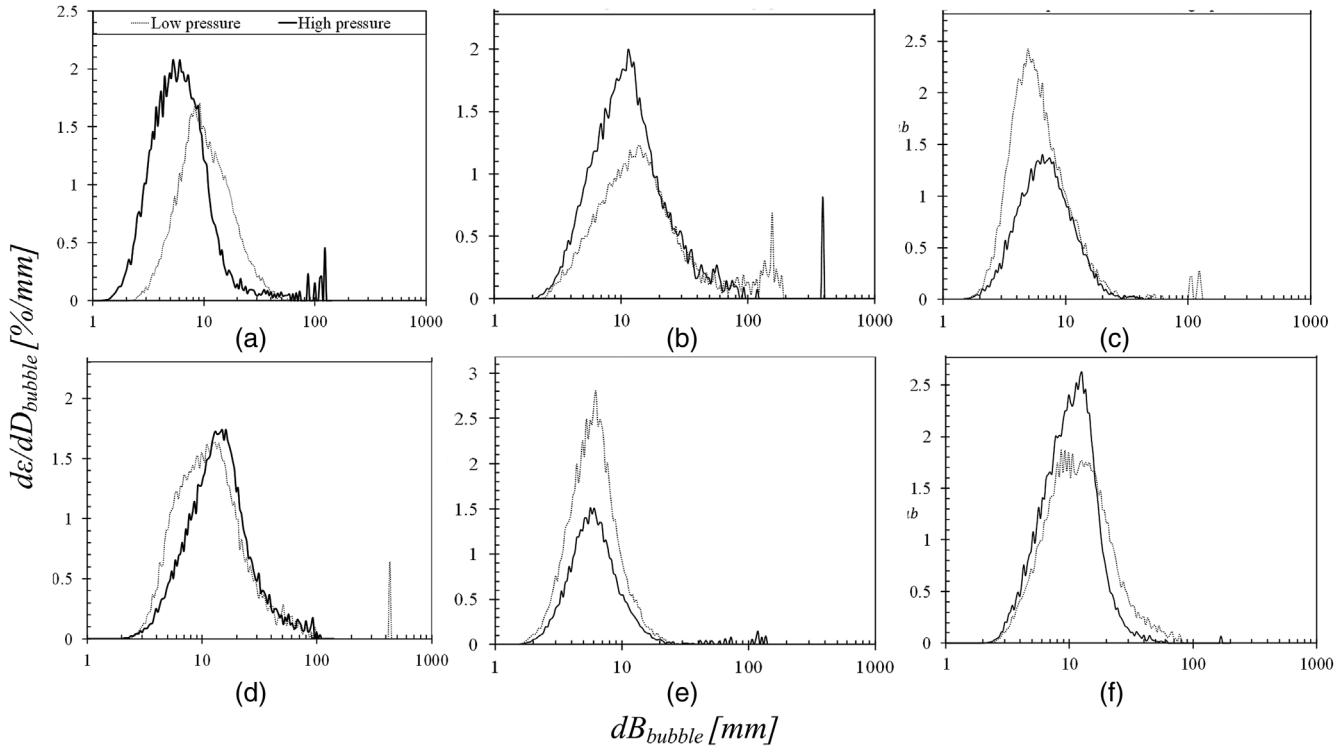

FIGURE 17 Some selected bubble size distribution plots at the following conditions: liquid and gas superficial velocities of (a) 0.2, 0.1, (b) 0.2, 0.6, (c) 0.4, 0.1, (d) 0.4, 0.6, (e) 0.6, 0.1, (f) 0.6, 0.6 m/s, respectively

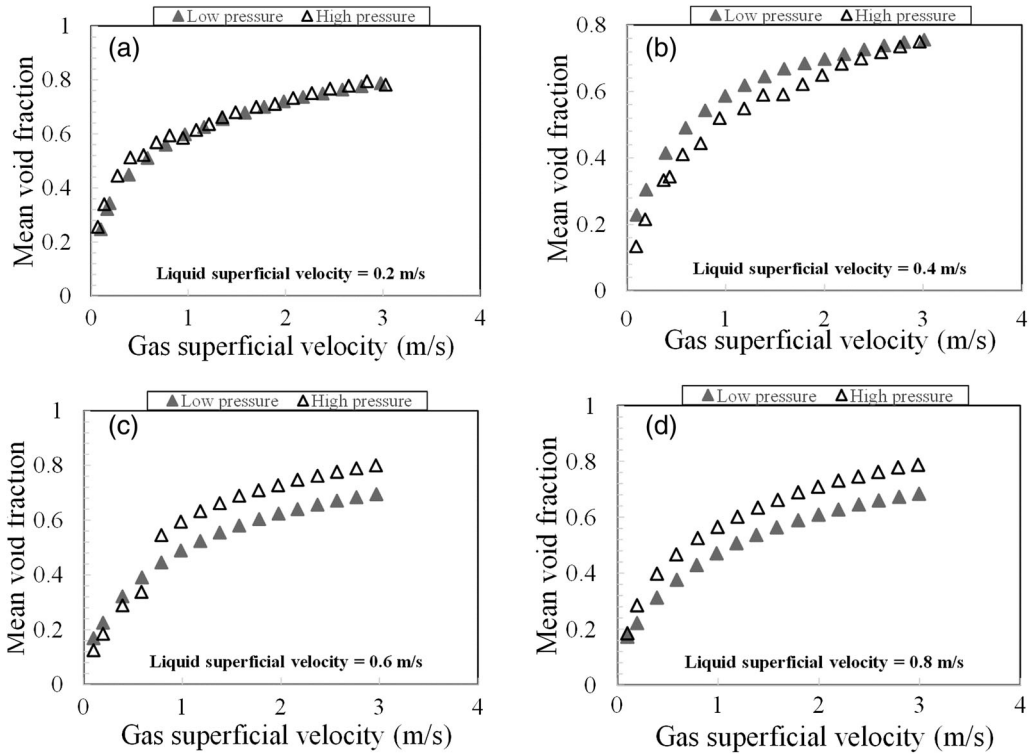

FIGURE 18 Effect of pressure on mean void fraction at different liquid and gas superficial velocities

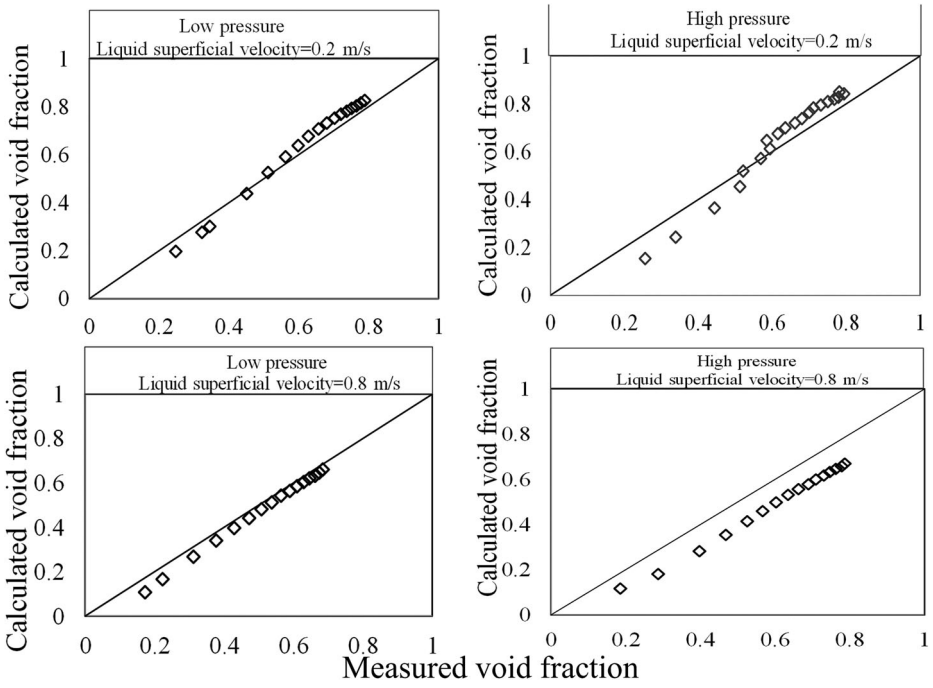

FIGURE 19 Comparison between experimental mean void fraction measured using wire mesh sensor (WMS) against mean void fraction calculated from differential pressure transducers (DPT)

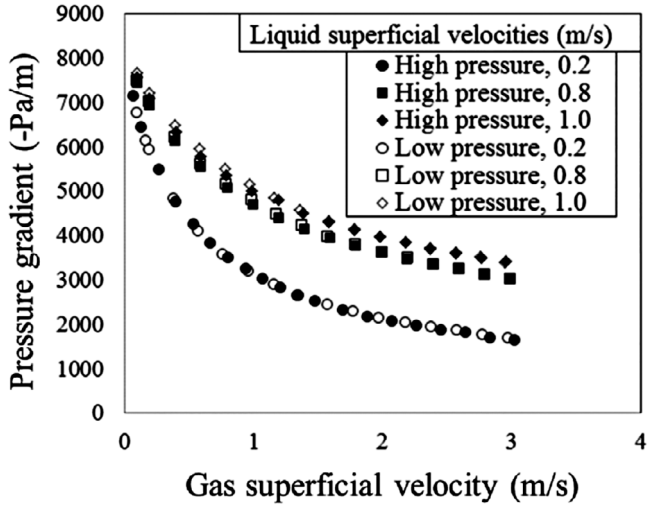

FIGURE 20 Pressure gradient relationship with gas superficial velocity

The calculated void fraction was derived from the relationship between total pressure gradient, gravitational pressure gradient, and frictional pressure gradient (assuming a steady state flow with acceleration pressure gradient equals zero).

In Figure 19, the void fraction calculated from $\frac{\frac{dP}{dz}-\rho_G g}{(\rho_L-\rho_G)g} = \frac{\overline{dP}_g-\rho_G}{(\rho_L-\rho_G)}$ as well as the measured void fraction were almost the same at low pressure; however, when the pressure was elevated, the difference became significant especially at low gas superficial velocities.

Where, g is the gravitational acceleration constant, DP/Dz is the pressure gradient and $\rho_L$and $\rho_G$are the densities of the liquid and gas, respectively.

The frictional component is rather small and the pressure gradient is almost determined by the gravitational one. On the other hand, when the pressure increases and velocity also increases, the frictional component cannot be neglected. Then gravitational component decreases and on the other hand frictional component increases. As expected, the pressure gradient increases with an increase in gas superficial velocity. Figure 19d suggests that the decrease in the gravitational component is significant than the increase in the frictional one. In addition, because we are operating in the bubble/churn flow regime, the gravitational component is expected to decrease with an increase in void fraction as a consequence of an increase in gas superficial velocity. This is in agreement with the observation of Owen.[1]

It can be observed from Figure 20 that the total pressure gradient decreases with an increase in gas superficial velocity for all the liquid superficial velocities considered. On the other hand, as expected, the total pressure gradient increases with an increase in liquid superficial velocity owing to an increase in mixture density. The observed decrease in the total pressure gradient can be described by the fact that the flow in the pipe is gravity dominated, that is, the major contributor to total pressure gradient in a vertical pipe is gravitational pressure gradient ($\rho_m g$). In addition, an increase in gas superficial velocity, will stimulate an increase in the void fraction, thereby reducing the mixture density as a result of a decrease in the liquid hold up (1—void fraction). However, the velocities encountered are not high enough to cause high frictional pressure gradients. Thus, the total pressure gradient decreases with an increase in gas superficial velocity. There is, however, no noticeable effect of pressure on the total pressure gradient.

In order to examine the effect of pressure on pressure gradient in greater details,[1] made a plot of dimensionless pressure gradient (representing y-axis) against the dimensionless air flowrate (x-axis) (see Figure 1). He defined the dimensionless pressure gradient and dimensionless air flow rate as follows:

$$\text{Dimensionless pressure gradient} = \frac{\frac{dP}{dz} - \rho_G g}{(\rho_L - \rho_G)g} = \frac{\frac{\partial P}{\partial z} - \rho_G}{(\rho_L - \rho_G)} \quad (7)$$

and

$$\text{Dimensionless air flow rate}, V_G{}^* = \frac{U^2}{gD} \quad (8)$$

The concept of Owen[1] was applied in this work in order to find the effect of pressure on pressure gradient. The plot showing this effect of pressure is depicted in Figure 21. It is worth mentioning, however, that the dimensionless air flow rate was replaced in this work using the Kutateladze number, *Ku*. *Ku* is defined mathematically in Equation 9

$$Ku = \frac{u_{sg}\rho_G{}^{0.5}}{([\rho_L - \rho_G]g\sigma)^{0.25}} \quad (9)$$

It can be observed from Figure 21 that the effect of pressure though not very significant is more pronounced using this axes.

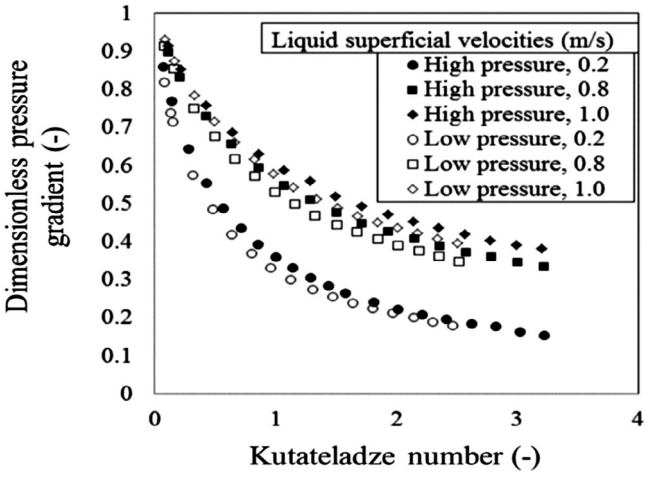

FIGURE 21 Dimensionless pressure gradient relationship with Kutateladze number

3.6 | Comparison of measured void fraction against other void fraction prediction models

The oil and gas industry has a great number of void fraction prediction models. Many of these models have been modified to fit into transient flows to effectively predict flow assurance and multiphase flows in terrain environments. For instance, OLGA for flow assurance as well as 1D LedaFlow and Maximus use some of these models in flow assurance predictions. Hence, it is imperative to carry out analysis based on these models in order to suggest ways of improving on the performance of the existing models as some of them have been observed to either under-predict or over-predict void fraction. In this section, comparisons will be made with three models reported in the literature at the conditions set for the experimental campaign. The models considered in this work are the homogeneous, CISE/Friedel, and the Beggs and Brill models.

Figures 22 and 23 show comparisons between the measured (experimental) void fraction against the homogeneous, CISE/Friedel, and the Beggs and Brill predicted void fraction models. In the case described in Figure 22, the liquid momentum was quite low and the predicted void fraction varies largely from those obtained from experiments. However, the CISE/Friedel and homogenous models over-predict void fraction at low liquid superficial velocity of 0.4 m/s and high gas superficial velocities while the Beggs and Brill's model under-predicts void fraction at liquid superficial velocity of 0.6 m/s. In Figure 23, the liquid momentum for the flow conditions is enhanced

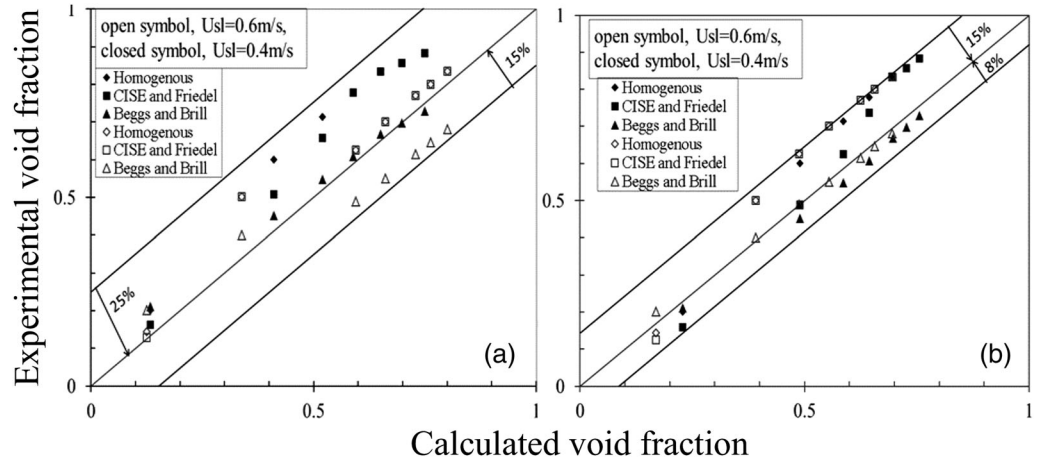

FIGURE 22 Comparison between the homogeneous, CISE/Friedel, and the Beggs and Brill models against experimental data at liquid superficial velocities of 0.4 m/s and 0.6 m/s. (a) High pressure. (b) Low pressure

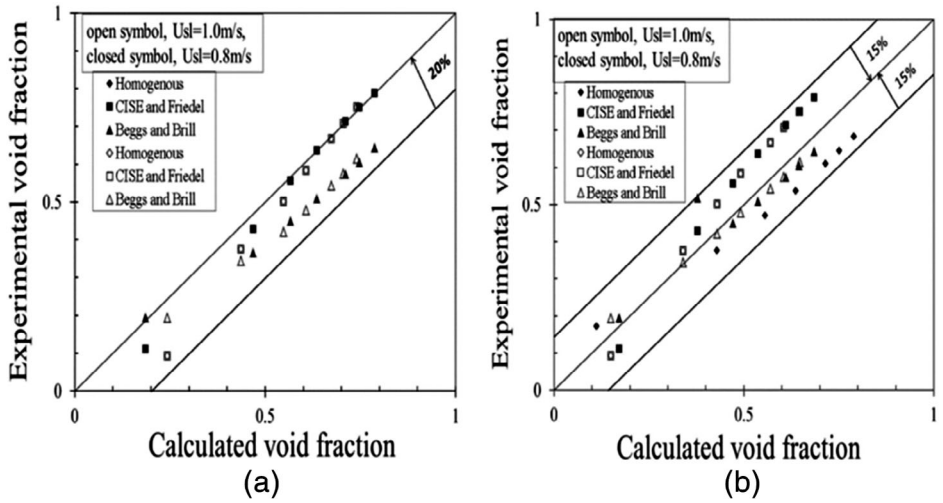

FIGURE 23 Comparison between the homogeneous, CISE/Friedel, and the Beggs and Brill models against experimental data at liquid superficial velocities of 0.8 m/s and 1.0 m/s. (a) High pressure. (b) Low pressure

to create better predictions for the various models. Both the homogenous and CISE/Friedel models perform well whereas Beggs and Brill's model over-predicts the void fraction.

In summary, the three considered models namely homogeneous, CISE/Friedel, and the Beggs and Brill are more effective especially at higher liquid superficial velocities. These are assumed to be the points at which the liquid momentum is high enough to avoid reverse flows that may occur at low liquid superficial velocities. In addition, the results show that the three models perform better at lower pressure than at high pressure. Generally, the void fraction data from experiment are within 15% of those predicted by the three models at low pressure but higher (between 20 and 25%) for high pressure. As reported by Szalinski et al,[11] these models perform well for oil of low viscosity but poorly with water with a lower viscosity; however, their performance with highly viscous liquid are not well understood.

4 | CONCLUSION

The article has presented the experimental results to study the effect of pressure on two-phase gas–viscous liquid flow at two pressure conditions, 4.5 and 7.5 bar in a vertical 127 mm internal diameter pipe. The system fluid is sulfur hexafluoride (SF6) with densities of 28 and 45 kg/m^3 and high viscosity oil mixture (mixture of Nexbase 3080 oil with viscosity of 89 mPa.s and Exssol D80 oil with viscosity of 1.76 mPa.s). The flow characteristics were measured and characterized using advanced instrumentation, including capacitance WMS and a differential pressure transducer. That the following conclusions can be drawn:

1. Dominant frequency increases with an increase in pressure. The dominant frequency also increases with liquid superficial velocity. This is in agreement with observations reported in the literature;
2. The plot of gas Strouhal number against Lockhart–Martinelli lie on a parallel line compared with most of the other data under consideration;
3. At low gas superficial velocity, there are no significant changes in bubble size distribution. However, wisps were observed at higher gas superficial velocities and at elevated pressures;
4. In the present work, wisps appear to be smaller, which might be due to the different fluid properties of the working fluids employed;
5. Wisps are easily revealed as long as there is a transition between churn and annular flows regardless of the pressure;
6. The effect of pressure on average void fraction at low liquid superficial velocities was found to be negligible while on the other hand, became significant at high liquid superficial velocities;
7. As the liquid superficial velocity increases, the calculated average void fraction shows some disagreement with measured void fraction;
8. The dimensionless pressure gradient relationship used by Owen[1] with a modification to the dimensionless air flowrate was used to find the effect of pressure;
9. Correlations of CISE/Friedel, homogeneous, and Beggs and Brill's perform well at high liquid superficial velocities when compared against measured void fraction. This could be attributed to higher momentum at higher liquid velocities. Better agreement was however observed for higher pressure than for lower pressure;
10. Viscosity effect can be moderated using dimensionless groups as these take into consideration different parameters that can affect two-phase flow.

ACKNOWLEDGMENT

M. Abdulkadir would like to express his sincere appreciation to the Nigerian government through the Petroleum Technology Development Fund (PTDF) for providing the funding for his doctoral studies. This work has been undertaken within the Joint Project on Transient Multiphase Flows and Flow Assurance. The author(s) wish to acknowledge the contributions made to this project by the UK Engineering and Physical Sciences Research Council (EPSRC) and the following: - ASCOMP, GL Noble Denton; BP Exploration; CD adapco; Chevron; ConocoPhillips; ENI; ExxonMobil; FEESA; FMC Technologies; IFP Energies nouvelles; Granherne; Institutt for Energiteknikk; Kongsberg

Oil & Gas Technologies; MSi Kenny; PDVSA (INTEVEP); Petrobras; PETRONAS; SPT Group; Shell; SINTEF; Statoil and TOTAL. The author(s) wish to express their sincere gratitude for this support. A. Abdulahi would like to thank University of Nottingham Graduate School for providing funding to travel to the SINTEF Multiphase Flow Laboratory, Trondheim, Norway under the BESTS Scholarship Scheme.

NOTATION

D	pipe diameter (m)
F_S	frequency of slug (Hz)
f_W	wisp frequency (Hz)
f	dominant frequency (Hz)
U_{SG}	gas superficial velocity (m/s)
U_{SL}	liquid superficial velocity (m/s)
V_{SL}	liquid superficial velocity (m/s)
V_M	mixture velocity (m/s)
SF_6	sulfur hexafluoride
AW150	air–water experiment in a 150 mm diameter pipe
AW67	air–water experiment in a 67 mm diameter pipe
AW194	air–water experiment in a 194 mm diameter pipe
ASiO67	air–silicone oil experiment in a 67 mm diameter pipe 150,194 and 67 mean corresponding pipe diameters
g	gravitational acceleration
PDF	probability density function
ECT	electrical capacitance tomography
WMS	wire mesh sensor
PSD	power spectral density
HP	high pressure (7.5 bar)
LP	low pressure (4.5 bar)
We	Weber number ($\frac{\rho v^2 D}{\sigma}$)
N_f	inverse viscosity number

GREEK LETTERS

ρ_l	liquid density (kg/m^3)
ρ_g	gas density (kg/m^3)

ORCID

Mukhtar Abdulkadir https://orcid.org/0000-0003-2308-9469

REFERENCES

1. Owen D. *An experimental and theoretical analysis of equilibrium annular flow* [PhD Thesis. Birmingham: University of Birmingham; 1986.
2. Hewitt GF. Churn and wispy annular flow regimes in vertical gas–liquid flows. *Energy Fuels*. 2012;26:4067-4077.
3. Nishikawa K, Sekoguchi T, Fukano T. On the pulsation phenomena in gas-liquid two-phase flow: relationship between pulsating pressure and flow pattern in upward two-phase flow. *Bull JSME*. 1969;12:1410-1416.
4. Cheng H, Hills JH, Azzorpardi BJ. A study of the bubble-to-slug transition in vertical gas-liquid flow in columns of different diameter. *Int J Multi Flow*. 1998;24:431-452.
5. Ohnuki A, Akimoto H. An experimental study on developing air-water two-phase flow along a large vertical pipe: effect of air injection method. *Int J Multi Flow*. 1996;22:1143-1154.
6. Jayanti S, Hewitt GF. Prediction of the slug-to-churn flow transition in vertical two-phase flow. *Int J Multi Flow*. 1992;18:847-860.
7. Taitel Y, Barnea D, Dukler AE. Modelling flow pattern transitions for steady upward gas-liquid flow in vertical tubes. *AIChE J*. 1980;26:345-354.
8. Costigan G, Whalley PB. Slug flow regime identification from dynamic void fraction measurements in vertical air-water flows. *Int J Multi Flow*. 1997;23:263-282.
9. Hernandez-Perez V. *Gas-liquid two-phase flow in inclined pipes* [PhD Thesis. Nottingham: University of Nottingham; 2008.
10. Hernandez–Perez V, Azzopardi BJ, Kaji R, da Silva MJ, Beyer M, Hampel U. Wisp-like structures in vertical gas–liquid pipe flow revealed by wire mesh sensor studies. *Int J Multi Flow*. 2010;36:908-915.
11. Szalinski L, Abdulkareem LA, Da Silva MJ, et al. Comparative study of gas–oil and gas–water two-phase flow in a vertical pipe. *Chem Eng Sci*. 2010;65:3836-3848.
12. Abdulkadir M, Azzi A, Zhao D, Lowndes IS, Azzopardi BJ. Liquid film thickness behaviour within a large diameter vertical 180° return bend. *Chem Eng Sci*. 2014;107:137-148.
13. Abdulkadir M, Hernandez-Perez V, Lowndes IS, Azzopardi BJ, Sam–Mbomah E. Experimental study of the hydrodynamic behaviour of slug flow in a horizontal pipe. *Chem Eng Sci*. 2016;156:147-161.
14. Abdulkadir M, Samson JN, Zhao D, Okhiria DU, Hernandez-Perez V. Annular liquid film thickness prediction in a vertical 180° bend. *Exper Therm Fluid Sci*. 2018;96:205-215.
15. Prasser HM, Bottger A, Zschau J. A new electrode-mesh tomograph for gas-liquid flows. *Flow Measurem Instrument*. 1998;9:111-119.
16. Prasser HM, Scholz D, Zippe C. Bubble size measurement using wire-mesh sensors. *Flow Measure Instrument*. 2001;12:299-312.
17. Prasser HM, Misawa M, Tiseanu I. Comparison between wire-mesh sensor and ultra-fast X-ray tomograph for an air–water flow in a vertical pipe. *Flow Measure Instrument*. 2005;16:73-83.
18. Prasser HM. Novel experimental measuring techniques required to provide data for CFD validation. *Nuclear Eng Des*. 2008;238:744-770.
19. Richter S, Aritomi M, HM HR. Approach towards spatial phase reconstruction in transient bubbly flow using a wire-mesh sensor. *Int J Heat Mass Trans*. 2002;45:1063-1075.
20. Krepper E, Lucas D, Prasser HM. On the modelling of bubbly flow in vertical pipes. *Nucl Eng Des*. 2005;235:597-611.
21. Manera A, Prasser HM, Lucas D, van der Hagen THJJ. Three dimensional flow pattern visualization and bubble size distributions in stationary and transient upward flashing flow. *Int J Multi Flow*. 2006;32:996-1016.
22. Azzopardi BJ. Flow patterns: does gas/solids flow pattern correspond to churn flow in gas/liquid flow. *Indus Eng Chem Res*. 2008;47:7934-7939.
23. Da Silva MJ, Schleicher E, Hampel U, Prasser HM. Patent: Grid sensor for the two-dimensional measurement of different components in the cross section of a multiphase flow. 2006; WO 2007121708, DE 102006019178.
24. Da Silva MJ, Schleicher E, Hampel U. Capacitance wire-mesh sensor for fast measurement of phase fraction distributions. *Measure Sci Tech*. 2007;18:2245-2251.
25. Da Silva MJ. *Impedance sensors for fast multiphase flow measurement and imaging* [PhD Thesis. Technische Universitat: Dresden; 2008.
26. Da Silva MJ, Thiele S, Abdulkareem L, Azzopardi BJ, Hampel U. High-resolution gas–oil two-phase flow visualization with a capacitance wire-mesh sensor. *Flow Measure Instrument*. 2010;21:191-197.
27. Thiele S, Da Silva, MJ, Hampel U, Abdulkareem L, Azzopardi BJ. High-resolution oil-gas two-phase flow measurement with a new capacitance wire-mesh tomography. 5th International Symposium on Process Tomography, Poland, Zakopane, 25–26 August 2008.

28. Azzopardi BJ, Abdulkareem LA, Zhao D, et al. Comparison between electrical capacitance tomography and wire mesh sensor output for air/silicone oil flow in a vertical pipe. *Indus Eng Chem Res*. 2010;49: 8805-8811.
29. Abdulkadir M, Hernandez-Perez V, Lowndes IS, Azzopardi BJ, Sharaf S. Experimental investigation of phase distributions of two-phase air–silicone oil flow in a vertical pipe. World Academy of Science. *Eng Tech (WASET)*. 2010;4:18-25.
30. Abdulkadir M, Hernandez–Perez V, Lowndes IS, Azzopardi BJ, Brantson ET. Detailed analysis of phase distributions in a vertical riser using wire mesh sensor (WMS). *Exp Thermal Fluid Sci*. 2014;59:32-42.
31. Abdulkadir M, Hernandez–Perez V, Kwatia CA, Azzopardi BJ. Interrogating flow development and phase distribution in vertical and horizontal pipes using advanced instrumentation. *Chem Eng Sci*. 2018; 186:152-167.
32. Pietruske H, Prasser HM. Wire-mesh sensors for high-resolving two-phase flow studies at high pressures and temperatures. *Flow Measure Instrument*. 2007;18:87-94.
33. Omebere-Iyari NK, Azzopardi BJ, Lucas D, Beyer M, Prasser HM. Gas/liquid flow in large risers. *Int J Multi Flow*. 2008;34:461-476.
34. Wangjiraniran W, Aritomi M, Kikura H, Motegi Y, Prasser HM. A study of non-symmetric air water flow using wire mesh sensor. *Exp Ther Fluid Sci*. 2005;29:315-322.
35. Fuangworawong N, Kikura H, Aritomi M, Komeno T. Tomographic imaging of counter-current bubbly flow by wire mesh tomography. *Chem Eng J*. 2007;130:111-118.
36. Ito D, Prasser HM, Kikura H, Aritomi M. Uncertainty and intrusiveness of three-layer wire-mesh sensor. *Flow Measure Instrument*. 2011; 22(4):249-256.
37. Pereyra E, Torres C. FLOPATN—Flow Pattern Prediction and Plotting Computer Code. In: Shoham O, ed. *Mechanistic Modelling of gas-liquid two-phase flow*. Society of Petroleum; 2005, 2006.
38. Gregory GA, Scott DS. Correlation of liquid slug velocity and frequency in horizontal cocurrent gas-liquid slug flow. *AIChE J*. 1969;15: 933-935.
39. Hubbard MG. *An analysis of horizontal gas-liquid slug* [PhD Thesis. Houston: University of Houston; 1965.
40. Bendat J, Piersol A. *Engineering application of correlation and spectral analysis*. New York: John Wiley & Sons, Inc.; 1980:1980.
41. Hubbard MG, Dukler AE. The characterization of flow regimes for horizontal two-phase flow, Proceedings of the 1966 Heat Transfer and Fluid Mechanics Institute, Stanford University Press. 1966; 100–121.
42. Gokcal B, Al-Sarkhi AS, Sarica C, Al-Safran EM. Prediction of slug frequency for high viscosity oils in horizontal pipes. SPE Annual Technical Conference and Exhibition, New Orleans, Lousiana, USA, 4–7 October 2009.
43. Sharaf S, van der Meulen GP, Azzopardi BJ, Reconciliation between two forms of churn flow in large diameter vertical pipes. 8th International Conference of Multiphase Flows, Jeju, Korea, 26–31 May 2013.
44. Prasser HM, Beyer M. Bubble recognition algorithm for the processing of wire mesh sensor data. 6th International Conference of Multiphase Flows, Leipzig, Germany, 9–13 July 2007.

How to cite this article: Abdulkadir M, Abdulahi A, Eastwick CN, Azzopardi BJ, Smith IE, Unander TE. Investigating the effect of pressure on a vertical two-phase upward flow with a high viscosity liquid. *AIChE J*. 2020;66: e16860. https://doi.org/10.1002/aic.16860